

The nature of the mistral: Observations and modelling of two MAP events

By QINGFANG JIANG¹*, RONALD B. SMITH¹ and JAMES DOYLE²

¹*Yale University, New Haven, USA*

²*Naval Research Laboratory, Monterey, USA*

(Received 28 January 2002; revised 2 August 2002)

SUMMARY

Two mistral events observed in 1999 during the Mesoscale Alpine Programme (MAP) are studied using observational data and high-resolution mesoscale-model simulations from the US Navy's Coupled Ocean Atmosphere Mesoscale Prediction System (COAMPS). Radiosondes suggested that both mistral wind events were associated with the passage of cold fronts and post-frontal air descent. EuroSat Rapidscan images indicated a stationary and persistent cloud edge along the lee of the Massif Central. The cloud edge marks the beginning of mistral flow acceleration and descent according to COAMPS simulations. Narrow persistent cloud banners were identified trailing from the Mont Lozère in the Massif Central during both mistral events. COAMPS indicated that these cloud banners were associated with a deeper turbulent boundary layer in wakes induced by hydraulic jumps. The cloud banner and wake defined the western boundary of the mistral.

Analysis of dropsonde data and *in situ* flight data indicated the presence of a sharp shear line separating the cold severe mistral wind from the warm calm wake flow to the lee of the French Alps. Trajectory analysis of model data suggested that air parcels on the two sides of the shear line had different histories.

KEYWORDS: Hydraulic jump Mesoscale Alpine Programme Mountain wake

1. INTRODUCTION

To many tourists, France is well known as 'the country of the mistral'. The term mistral refers to a severe wind that develops along the Rhône Valley and influences the Mediterranean coast of south-eastern France (Fig. 1). While the mistral makes the eastern French coast a windsurfer's paradise, it is also considered the most dangerous of all the Mediterranean winds because of its severity and persistence. Strong mistral may extend into the western and central Mediterranean and through the Strait of Bonifacio (between the islands of Corsica and Sardinia). It creates high sea states throughout the entire region, and contributes to the Mediterranean deep-water formation by cooling the sea surface (Schott *et al.* 1996).

To local forecasters, the development of the mistral is preconditioned by cyclogenesis over the Gulf of Genoa and the passage of a trough through France. In earlier interpretations, the mistral mechanism was described as cold air funnelling through the Rhône Valley or fall wind (Galzi 1952; Gerbier and Berenger 1961; Bordreuil *et al.* 1973; Mayencon 1980; Wrathall 1985). However, most literature on this subject has been descriptive rather than mechanistic. Little is known about the dynamical details and the roles of mesoscale terrain in the mistral development and evolution. In contrast, the eastern analogy to the mistral, the Bora, has been more fully studied. Bora is the cold north-easterly flow reaching the Mediterranean Sea around the eastern end of the Alps (Smith 1987). The acceleration of the Bora over the coastal range of the Adriatic was shown to arise from pressure gradients caused by a shallow descending inversion, sometimes decoupled from the flow aloft by a critical layer.

A field experiment, known as 'Campagne vallée du Rhône 77', was carried out to look at the structure of the mistral flow along the Rhône Valley (Pettre 1982). Six northerly wind events were documented during a month-long field period. Warming of the air and flow descent from north to south were observed. The distribution of the

* Corresponding author: Naval Research Laboratory, 7 Grace Hopper Ave., Monterey, CA 93943-5502, USA.
e-mail: jiang@nrlmry.navy.mil

Report Documentation Page				Form Approved OMB No. 0704-0188	
Public reporting burden for the collection of information is estimated to average 1 hour per response, including the time for reviewing instructions, searching existing data sources, gathering and maintaining the data needed, and completing and reviewing the collection of information. Send comments regarding this burden estimate or any other aspect of this collection of information, including suggestions for reducing this burden, to Washington Headquarters Services, Directorate for Information Operations and Reports, 1215 Jefferson Davis Highway, Suite 1204, Arlington VA 22202-4302. Respondents should be aware that notwithstanding any other provision of law, no person shall be subject to a penalty for failing to comply with a collection of information if it does not display a currently valid OMB control number.					
1. REPORT DATE 02 AUG 2002		2. REPORT TYPE		3. DATES COVERED 00-00-2002 to 00-00-2002	
4. TITLE AND SUBTITLE The nature of the mistral: Observations and modelling of two MAP events				5a. CONTRACT NUMBER	
				5b. GRANT NUMBER	
				5c. PROGRAM ELEMENT NUMBER	
6. AUTHOR(S)				5d. PROJECT NUMBER	
				5e. TASK NUMBER	
				5f. WORK UNIT NUMBER	
7. PERFORMING ORGANIZATION NAME(S) AND ADDRESS(ES) Naval Research Laboratory, 7 Grace Hopper Ave., Stop 2, Monterey, CA, 93943-5502				8. PERFORMING ORGANIZATION REPORT NUMBER	
9. SPONSORING/MONITORING AGENCY NAME(S) AND ADDRESS(ES)				10. SPONSOR/MONITOR'S ACRONYM(S)	
				11. SPONSOR/MONITOR'S REPORT NUMBER(S)	
12. DISTRIBUTION/AVAILABILITY STATEMENT Approved for public release; distribution unlimited					
13. SUPPLEMENTARY NOTES					
14. ABSTRACT					
15. SUBJECT TERMS					
16. SECURITY CLASSIFICATION OF:			17. LIMITATION OF ABSTRACT Same as Report (SAR)	18. NUMBER OF PAGES 19	19a. NAME OF RESPONSIBLE PERSON
a. REPORT unclassified	b. ABSTRACT unclassified	c. THIS PAGE unclassified			

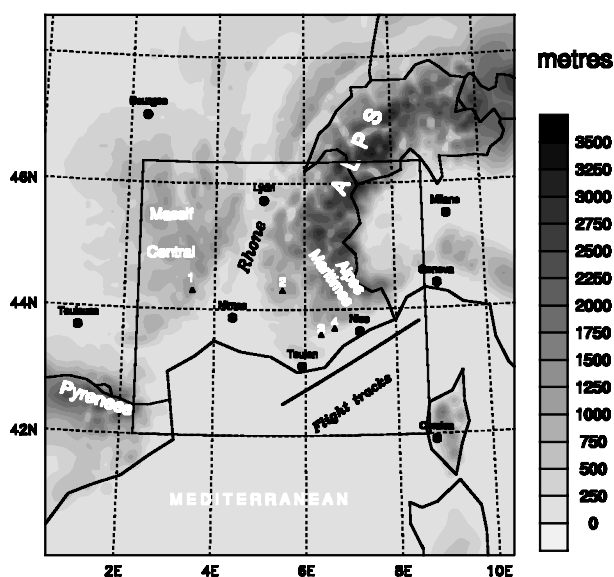


Figure 1. The Coupled Ocean Atmosphere Mesoscale Prediction System (COAMPS) 6 km and 2 km mesh computational-domain terrain field with coastline, political boundaries and geographical locations of interest. Research aircraft flight track is denoted by the solid line. Mountain peaks of interest are numbered: 1—Mont Lozère, 2—de Lure, 3—Mourre de Chanier, 4—Sommet dela Bernarde.

mistral over the sea surface was studied by Jansá (1987) based on an Advanced Very High Resolution Radiometer (AVHRR) image. A shear line was found that separated the severe mistral flow from the relatively calm flow to the lee of the Alps.

The revolutionary advances in remote-sensing technology, computer power and numerical tools, and mountain-flow theories over the past two decades allow us now to look at the mistral wind more closely and from a broader perspective. The Mesoscale Alpine Programme (Bougeault *et al.* 2001) provided a unique opportunity in this regard. Two mistral events were well documented during the MAP Special Observing Period (SOP). For the purpose of comparison, the two mistral events are presented side by side wherever it is possible. The primary objective of this study is to examine the structure and dynamics of the mistral wind, including the role of mesoscale terrain in the mistral formation. The paper is organized as follows. The synoptic background is reviewed in section 2. Radiosonde data is analysed in section 3. Rapidsan image analysis is presented in section 4. In section 5, dropsonde data and flight-level data are analysed. Numerical simulations are diagnosed in section 6. This study is summarized in section 7.

2. MAP AND THE MISTRAL IOPS

During the MAP SOP period (16 September–16 November 1999), two mistral events were well documented. The first mistral event was observed on 1 October 1999 (Intensive Observing Period (IOP) 4). Figure 2(a) shows the geopotential-height contours and horizontal wind field at 500 mb for 1200 UTC, 1 October 1999 based on Navy Operational Global Atmospheric Prediction System (NOGAPS) analysis dataset. A deep trough passed the Alps region followed by strong north-westerly flow. A surface low deepened over the Mediterranean which increased the pressure gradient across the Alps. These features were associated with the development of a pronounced shallow mistral flow, which lasted a few hours, from early morning to early afternoon.

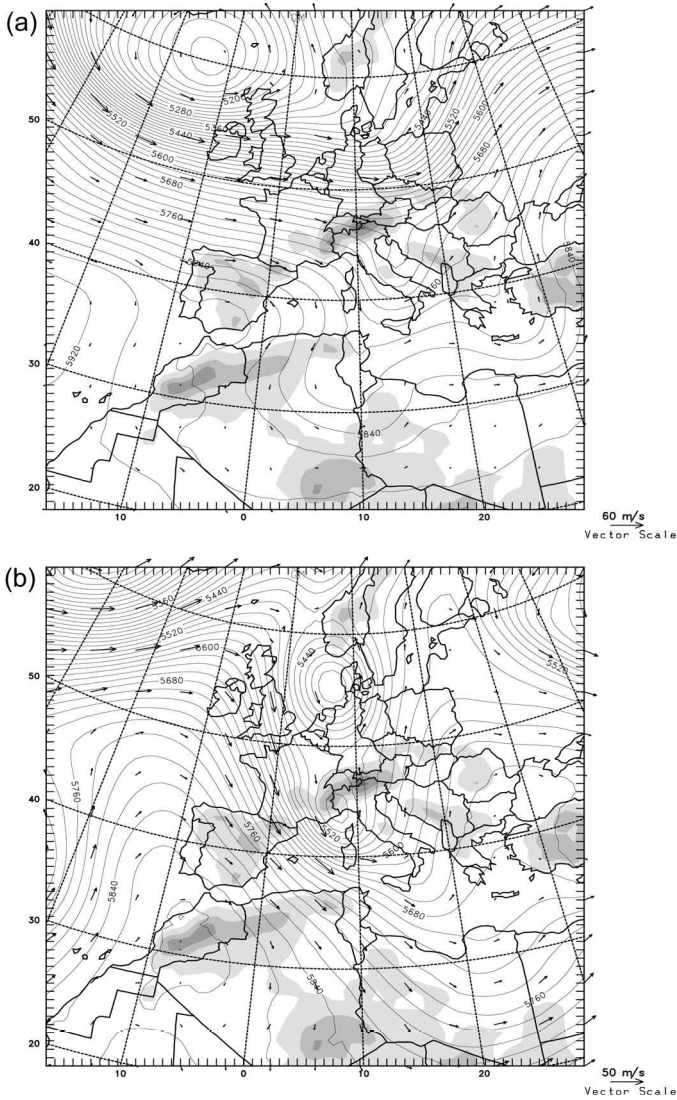


Figure 2. Geopotential height and wind vectors at 500 mb at (a) 1200 UTC, 1 October 1999 and (b) 1800 UTC, 6 November 1999, based on analyses from the Navy Operational Global Atmospheric Prediction System (NOGAPS).

Two aircraft, the National Center for Atmospheric Research (NCAR) Electra and the National Oceanic and Atmospheric Administration (NOAA) P-3, flew a stack pattern cutting through the forecasted shear line downstream of the French Alps (see Fig. 1 for the flight track and terrain). Besides *in situ* observations, the Electra down-looking lidar (SABL) and P-3 belly radar provided strong returns. Six dropsondes were dropped from the Electra along its first leg.

The second mistral event was observed on 6 November 1999 (IOP 15). The strong cold-air advection associated with a trough reached the Mediterranean in the morning of 6 November, followed by rapid cyclogenesis over the south-western Po Valley (Fig. 2(b)). The strength of the mistral peaked in the late afternoon. Again, both the

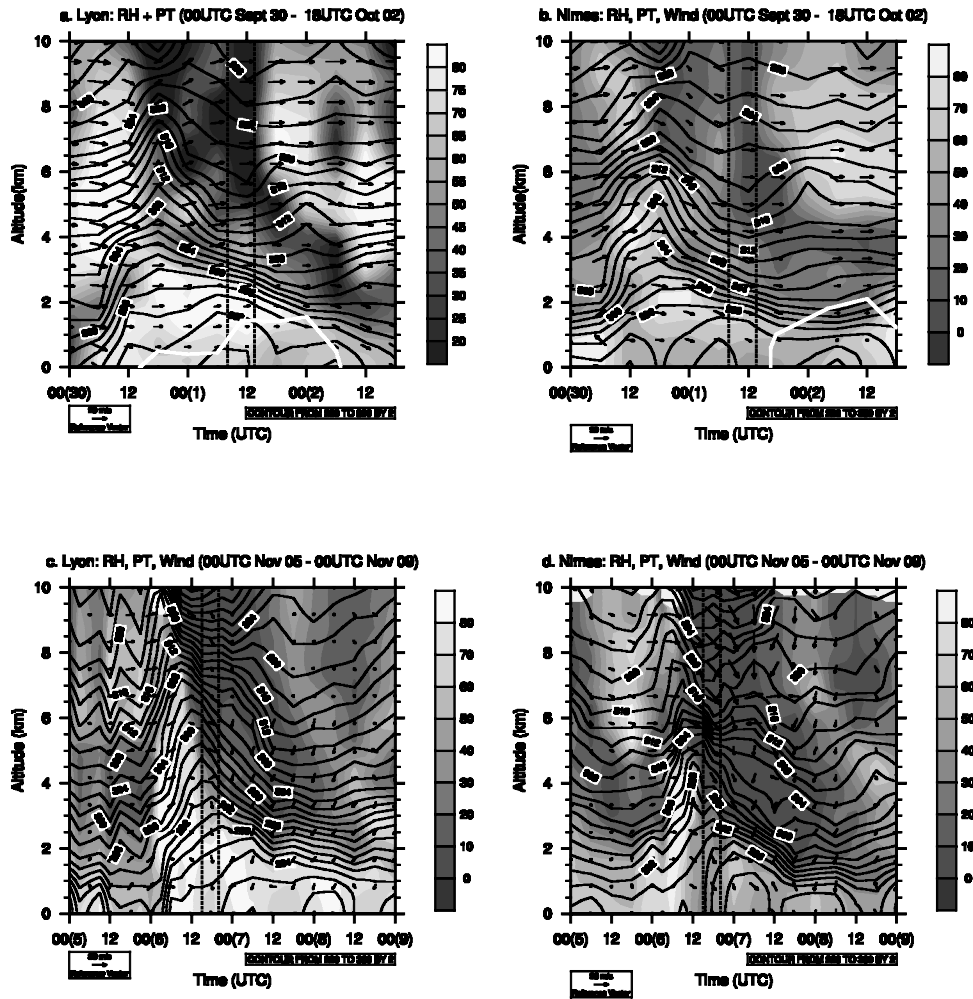


Figure 3. Hovmöller diagrams (height versus time) of potential temperature (PT, contours (K)), relative humidity (RH, grey scale (%)) and wind vectors (m s^{-1}) derived from radiosonde data at stations Lyon ((a) and (c)) and Nimes ((b) and (d)). Time runs from 0000 UTC, 30 September to 1800 UTC, 2 October for the first mistral event ((a) and (b)) and from 0000 UTC, 5 November to 0000 UTC, 9 November for the second mistral event ((c) and (d)). The aircraft flying periods are indicated by dashed lines. White lines are 5 m s^{-1} contours of wind speed, below which the wind speed is less than 5 m s^{-1} .

NCAR Electra and NOAA P-3 flew along the same flight track across the shear line and 14 dropsondes were dropped from the Electra along its two legs.

3. RADIOSONDE TIME SERIES

To examine the vertical structure of the mistral wind and its evolution, Hovmöller diagrams (height versus time) of potential temperature, humidity and wind are created using radiosonde data from two stations, Lyon and Nimes. Lyon (5.08°E , 45.73°N , 240 m above sea level (ASL)) is located at the entrance of the Rhône Valley, about 240 km from the Mediterranean coast. Nimes (4.4°E , 43.85°N , 59 m ASL) is located in the Rhône Valley and in the mistral wind (Fig. 1). While the regular observational

interval is 6 hours for both stations, the interval was reduced to 3 hours during a 24 h period, for each mistral.

The Hovmüller diagrams for Lyon and Nîmes for the period of 0000 UTC, 30 September to 1800 UTC, 2 October are shown in Figs. 3(a) and 3(b). A cold front passed Lyon around 1000 UTC, 30 September, followed by strong isentropic descent (Fig. 3(a)). The interface between the cold and warm air descended more than 2 km in less than 24 h, and became sharper and stronger. Above the inversion, the warm air was drier (relative humidity (RH) < 50%) and less stable. The research flight for this mistral event was from 0830 UTC to 1330 UTC, 1 October, during which the interface was descending. The most striking feature was the low-level blocking at Lyon (Fig. 3(a)). During the time period of the aircraft observations, wind speed below the inversion was less than 5 m s^{-1} . Similar features were observed at Nîmes (Fig. 3(b)) except that the wind speed under the inversion was much faster ($\sim 12 \text{ m s}^{-1}$) during the observing period. The air stream passing Nîmes was generally drier and the inversion at Nîmes was lower than at Lyon during the mistral period. For example, at 1200 UTC, 1 October, the 300 K isentrope was at 2300 m ASL at Lyon, and 2000 m ASL at Nîmes.

Hovmüller diagrams for the second mistral event are plotted in Figs. 3(c) and 3(d). The period is from 0000 UTC of 5 November to 0000 UTC of 9 November. Figure 3(c) shows that a cold front arrived at Lyon in the early morning around 0300 UTC, 6 November. After the passage of the cold nose, there was a rapid descent of the interface: a stable layer which separated the less stable warm air above and near-neutral cold air below. From 1600 UTC, 6 November to 1400 UTC, 7 November, the interface descended more than 2 km. For example, the 300 K isentrope descended from 5.5 km to 3.2 km. Above the interface, a deep dry layer extended from the interface to 10 km with relative humidity less than 15%. The cold air below was moist with relative humidity above 70%. The stratification observed at Nîmes (Fig. 3(d)) was quite similar with some exceptions. Nîmes saw a stronger descent and correspondingly the air above was drier and warmer.

4. RAPIDSCAN-DATA ANALYSIS

During the MAP SOP periods, Rapidscans of the Meteosat-6 standby satellite over the Alpine region had been activated by the European Meteorological Satellite system. Snapshots of the whole Alpine area were taken every 5 minutes over a period of 24 hours for every IOP. This unique dataset provided three-dimensional (i.e. x , y , t) information on cloud distribution and movement in this area. For this study, we focus on an area between 1.5°E to 9°E and 40°N to 47.5°N . These images included three channels; visible, infrared, and water vapour. The visible channel has the highest spatial resolution. However, for the second event, the mistral wind was not fully developed until the late afternoon when it was too dark for the visible channel. Therefore, in this study we use the visible channel for the 1 October event, and the infrared channel for the 6 November event.

Two images taken during the two mistral periods are shown in Figs. 4(a) and 4(b) as examples. For the first mistral (Fig. 4(a)), we can see a dark line running along the lee of the Massif Central peaks (indicated by a black arrow), with most clouds confined to the north-western side of the line. To the south-east, there was a vast area with clear sky except for isolated patches of clouds. Hereafter, we refer to this line as the Massif Central Clearing Line (MCCL, see Table 1 for description of abbreviations). Several cloud clusters can be seen downstream (i.e. to the south-east) of the MCCL. There were periodic lee-wave clouds lying to the south-west of Mont Lozère (1702 m)

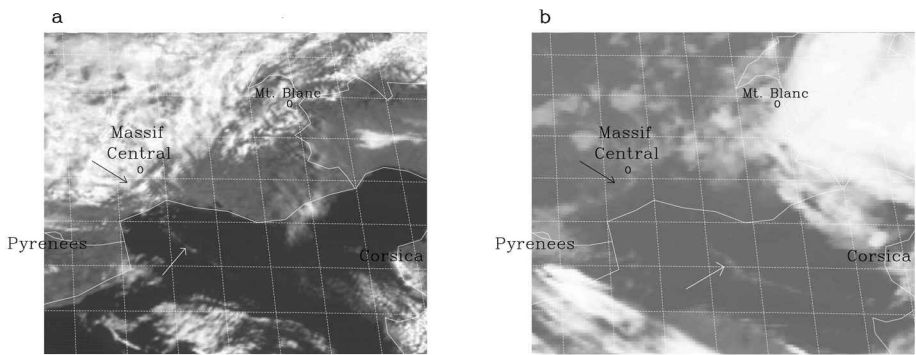


Figure 4. Rapidscan images. (a) Visible image at 1200 UTC, 1 October 1999. (b) Infrared image at 1800 UTC, 6 November 1999. The black arrow points to the Massif Central Clearing Line (MCCL) and the white arrow points to the Mont Lozère Banner Clouds (MLBC).

TABLE 1. LIST OF ABBREVIATIONS

Abbreviation	Description
MESL	Mistral Eastern Shear Line
MLBC	Mont Lozère Banner Clouds
MCCL	Massif Central Clearing Line
WAW	Western Alps Wake
MLW	Mont Lozère Wake

and parallel to the MCCL between the coastline and the MCCL. It is well known that the formation of trapped lee waves requires a sharp decrease of Scorer’s parameter ($l = N/U$) with altitude. For the first mistral event, as indicated by the sounding at Lyon, there was a strong inversion between 2 and 3 kilometres. Further aloft, the stability (N) decreased sharply and the cross-mountain wind speed (U) increased with altitude. Such a combination of stratification and wind speed was consistent with the lee waves found downstream from the cloud edge.

Two large cloud patches trailed from the Pyrenees and Maritime Alps. Another interesting feature was the narrow cloud filament oriented roughly along the wind direction (Fig. 4(a), indicated by a white arrow). This cloud filament seemed to emanate from Mont Lozère and extended more than 200 km downstream with a width of around 10 km. Hereafter, we refer to this cloud filament as the Mont Lozère Banner Clouds (MLBC). The characteristics and implication of the MLBC will be further examined later.

An image taken during the second mistral is shown in Fig. 4(b). High clouds can be seen over the leeward side of the Alps associated with the development of the Genova cyclone. While the cloud patterns were quite different from the earlier case (Fig. 4(a)), some interesting similarities can be seen. The same MCCL identified from Fig. 4(a) is clearly apparent (indicated by a black arrow), separating the upstream low clouds and the downstream clear area. This clear area was probably associated with low-level air descent. Based on mass-conservation principles, air descent may be associated with the acceleration of low-level flow. If this is true, the MCCL marked the beginning of the mistral acceleration. In the middle of the clear area, we can see narrow banner clouds (MLBC) extending more than 200 km downstream. The MLBC separated the clear area into two parts, where the mistral and the Tramontane winds are traditionally defined

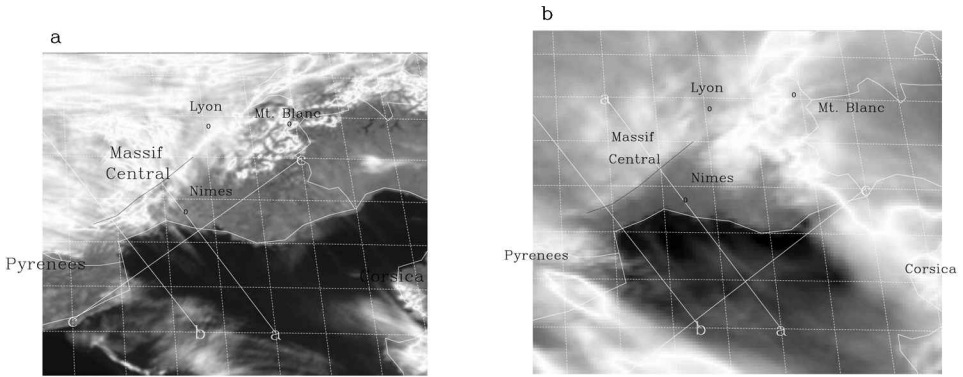


Figure 5. Composite images for (a) 0830–1200 UTC, 1 October 1999. (b) 1500–2400 UTC, 6 November 1999. The Massif Central Clearing Line (MCCL) is indicated by a thin dark line and three white lines, aa, bb, cc are marked for Hovmöller diagrams (Fig. 6).

(e.g. Campins *et al.* 1995). No evidence of lee waves was found during the second mistral. Radiosonde data indicated that the stable layer above the cold air during the second mistral event was much weaker. This might have allowed more wave energy to penetrate through the stable layer.

To examine the persistence of these features, composite images for the two mistral events are created by superposing all available snapshots over each mistral period (Figs. 5(a) and 5(b)). The MCCL identified from those snapshots is marked on both figures as a thin dark line. For reference, this line runs through the following points: (43.4°N, 2.5°E), (43.6°N, 3°E), (44.0°N, 3.45°E), (44.4°N, 4°E), and (45.0°N, 4.65°E). Some features observed in the snapshots are more pronounced in the composite images. For example, for both events, the MCCL is clearly seen in the composite images indicating that the MCCL was persistent and stationary though the two mistral events. Figure 5(a) shows several wave clouds to the west of Mont Lozère. During both events, persistent cloud streets extended from the Pyrenees to more than 200 km downstream. Figure 5(a) also shows the banner clouds (MLBC) indicating that for the first mistral the MLBC was fairly steady. The MLBC is not evident in Fig. 5(b), however.

To further examine the evolution of these clouds, Hovmöller diagrams, i.e. plots of distance versus time, are created along three lines, i.e. aa, bb, cc (see Fig. 5 for locations). Lines aa and bb transect the Massif Central roughly along the wind direction, and line cc is intended to pass across the MLBC observed in the snapshots (Fig. 4). For the first mistral, the upstream wind speed was approximately 10 m s^{-1} (Fig. 6(a)). Upstream propagating waves with wavelengths of approximately 15 km were evident. The MCCL was located about 60 km upstream of the coastline, clearly offshore except for the clouds trailing from the Pyrenees. The Hovmöller diagram along line aa (not shown) also indicated that the MCCL was stationary during the first mistral. Figure 6(b) shows that the MLBC was quite stationary and existed through most of the observed period. For the second mistral, the upstream wind speed (Fig. 6(c)), was approximately 20 m s^{-1} which agrees well with the radiosonde data analysis. The MCCL was stationary and located about 140 km upstream of the coastline. Similarly, the Hovmöller diagram along line bb (not shown) indicated a stationary MCCL. Figure 6(d) indicated that the MLBC was persistent, but not stationary. It drifted roughly westward at a constant speed of 6 m s^{-1} explaining the absence of MLBC in the composite image (Fig. 6(a)).

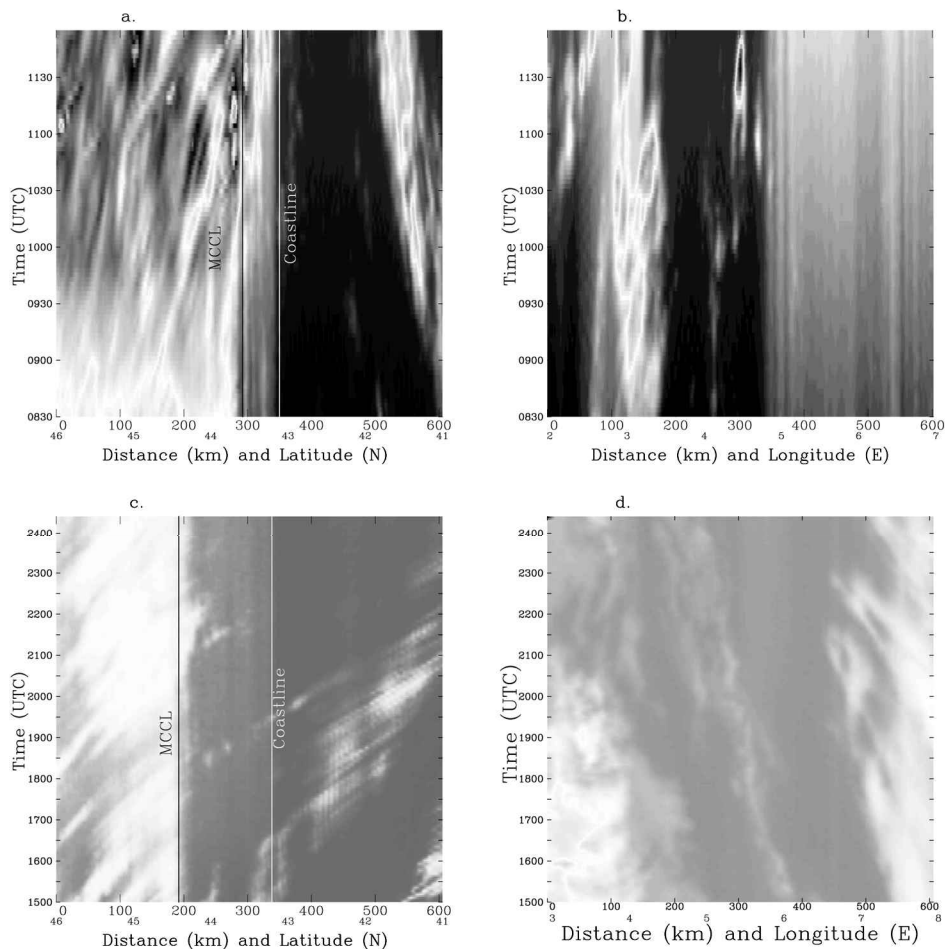


Figure 6. Hovmöller diagrams from Rapsiscan satellite data. (a) Along line bb for the first mistral (1 October 1999); (b) along line cc for the first mistral; (c) along line aa for the second mistral (6 November 1999); (d) along line cc for the second mistral. See Fig. 5 for locations of aa, bb, and cc. MCCL = Massif Central Clearing Line.

5. THE STRUCTURE OF THE MISTRAL EASTERN SHEAR LINE

One objective of MAP was to investigate the structure of the shear line downstream of the French Alps, i.e. the Mistral Eastern Shear Line (MESL), and associated potential-vorticity patterns (Aebischer and Schär 1998).

During the first mistral event, the Electra flew three legs (i.e. leg 1 ~ 4800 m, leg 2 ~ 360 m, and leg 4 ~ 1800 m ASL, respectively) along the indicated track (Fig. 1), and six Global Positioning System dropsondes were deployed during the first leg. During the second mistral event, the Electra flew two legs (i.e. leg 1 ~ 3800 m and leg 2 ~ 3000 m ASL) along the same track, and seven dropsondes were deployed along each leg.

(a) Dropsonde-data analysis

The vertical section constructed from an objective analysis of the six dropsonde measurements is shown in Fig. 7. The mistral wind was quite shallow (below 2 km) with a wind-speed maximum of about 20 m s⁻¹ near the sea surface. The wake with slow

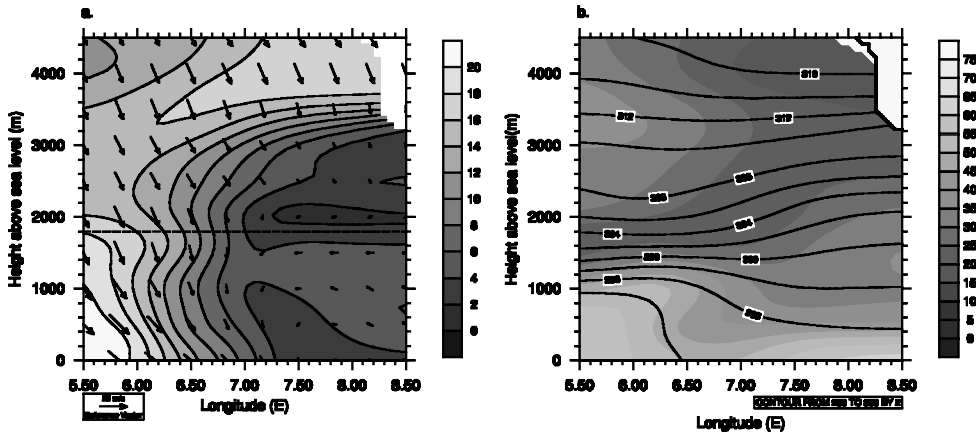


Figure 7. The vertical section along the flight track (see Fig. 1) for the first mistral (1 October 1999) derived from objective analysis of dropsonde data. (a) Horizontal wind vector and wind speed (m s^{-1} , grey scale). The flight level of leg 4 is shown as a dashed line; (b) potential temperature (K) is contoured and relative humidity (%) is given by the grey scale.

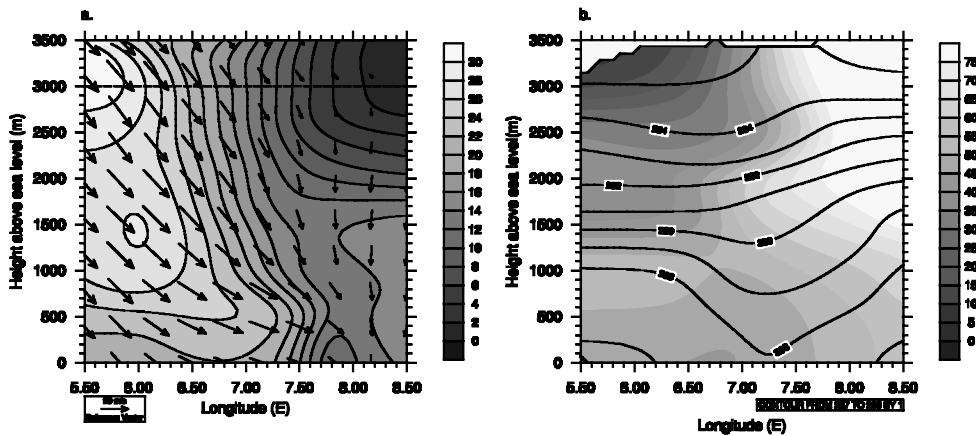


Figure 8. Same as Fig. 7 except for the second mistral (6 November 1999). The flight level of leg two is shown in (a) as a dashed line.

reversed flow was rather deep, reaching about 3 km. The maximum shear in terms of wind speed was located at 6.5°E . There was an inversion between 1 and 2 km ASL. The air above the inversion was much drier than air in the mistral, consistent with radiosonde data (section 3). Near the sea surface, the wake flow was more moist and about 2 K warmer than the mistral flow. There was a sharp decrease of RH with height in the wake flow, suggesting a moisture source at the sea surface. In contrast, RH in the mistral flow was rather uniform. In summary, this vertical section confirms the existence of the MESL. The dropsondes suggest that the mistral flow and wake flow had quite different properties in terms of stability, moisture content and wind.

The vertical section constructed from an objective analysis of the measurements from seven dropsondes during the first leg of the second mistral flight is shown in Fig. 8. Figures 8(a) and 8(b) indicate that the second mistral was much deeper and stronger with a wind-speed maximum exceeding 30 m s^{-1} at about 3 km to 3.5 km

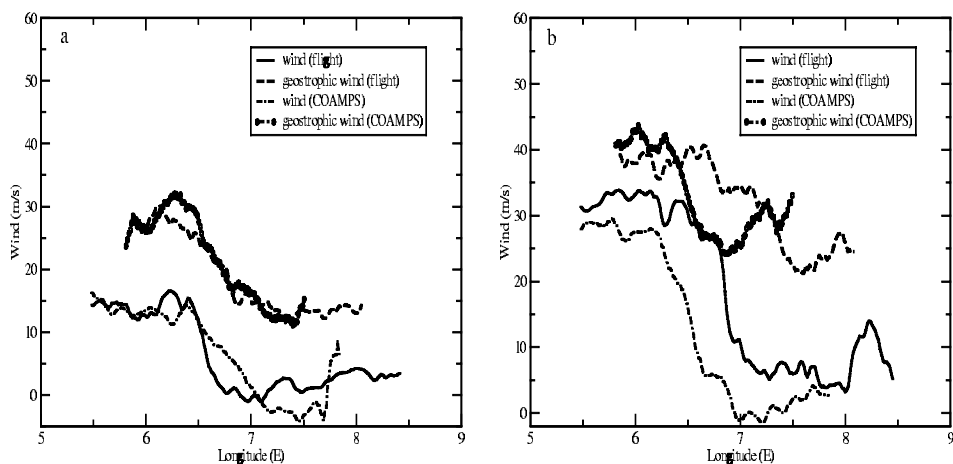


Figure 9. The measured wind and geostrophic wind in the direction normal to the flight track. The same quantities derived from the Coupled Ocean Atmosphere Mesoscale Prediction System (COAMPS) simulations are plotted for comparison. (a) Leg 4 of Electra flight, 1 October 1999. (b) Leg 2 of Electra flight, 6 November 1999.

ASL. A second maximum ($\sim 28 \text{ m s}^{-1}$) was located at 1.5 km ASL. A sharp shear line was present across which the wind direction changed from north-westerly in the mistral to northerly in the wake. Near the sea surface, the maximum shear occurred at 7.5°E , tilting to 6.75°E at 3.5 km ASL. We see a relatively stable layer between 1.25 km and 1.7 km, which separated the mistral wind into two less stable layers. The air above the stable layer was much drier. A moist wake core was located aloft (8.5°E and 3 km ASL) indicating a different air-mass source. Analysis of the dropsonde data during the second leg (not shown) showed similar features except that the shear zone was shifted about 0.3° to the west.

(b) Flight-data analysis

As an example, some data from the last leg of the first mistral flight is shown in Fig. 9(a). The measured wind and derived geostrophic wind component normal to the flight track are plotted as a function of longitude. The geostrophic wind is derived from static pressure and geometric radar altitude assuming hydrostatic balance.

Figure 9(a) shows strong shear near 6.5°E where wind speed dropped from 15 m s^{-1} to zero within about 0.35 degrees of longitude (i.e. 25 km). The wind direction reversed to the east of the MESL. The derived geostrophic wind was almost twice as strong as the measured wind, which indicated that the mistral flow at that level departed from geostrophic balance. To diagnose the observed ageostrophy, one should consider the acceleration (e.g. curvature) and friction. Previous observations (Jansá 1987) and Coupled Ocean Atmosphere Mesoscale Prediction System (COAMPS) simulations from these cases (section 6) indicated that the mistral flow had a cyclonic curvature near the coastline. If the radius of the curvature was around 200 km, the centrifugal force would be able to balance the additional pressure-gradient force. Friction is neglected in the above discussion for the following reasons. Flight leg 4 was 1800 m ASL where friction is considered less important. The measured average wind direction (160°N) was roughly normal to the flight track (60°N), thus, the along-flight-track component of the friction should be small.

A similar plot for the second Electra flight leg of the second mistral flight is shown in Fig. 9(b). The maximum mistral wind reached 34 m s^{-1} . The shear line was located near 6.75°E where the wind speed was reduced from 25 m s^{-1} to less than 7 m s^{-1} within 0.2 degrees of longitude. A second jet can be seen further east. Again, the geostrophic wind was about 20–30% stronger than the measured wind indicating that the mistral flow departed from geostrophy. The radius of curvature to the left should be around 800 km to maintain gradient balance. The analysis of other Electra and P-3 legs indicated that the strength and location of the shear line (MESL) varied rapidly with time. Generally, the MESL tended to shift westward in the late afternoon which agrees with the Rapidscan analysis (Fig. 6(d)).

It should be pointed out that the MESL based on dropsonde-data analysis (Figs. 7 and 8) appears broader than in the flight-data analysis (Fig. 9) as the dropsonde data had poorer horizontal resolution ($\sim 50 \text{ km}$). A combined aircraft and dropsonde analysis for the first case is given by Schär *et al.* (2003).

6. NUMERICAL SIMULATIONS AND DYNAMICS

(a) Numerical set-up

The atmospheric component of the Navy's COAMPS model (Hodur 1997) was used to simulate the two mistral events. COAMPS is a fully compressible, non-hydrostatic model with physical parametrizations such as long-/short- wave radiation (Harshvardhan *et al.* 1987), 1.5-order turbulent kinetic energy (TKE) closure (Mellor and Yamada 1974), and cloud microphysics.

The computational domain for the present study was configured with four horizontally nested grids of 73×61 , 97×97 , 133×133 , and 235×235 points. The corresponding horizontal spatial resolutions (Δx) are 36 km, 18 km, 6 km, and 2 km, respectively. The topographic data was taken from the US Defense Mapping Agency's 100 m resolution dataset. The model terrain fields for the third ($\Delta x = 6 \text{ km}$) and fourth meshes ($\Delta x = 2 \text{ km}$) are shown in Fig. 1. The fourth mesh includes the Massif Central, French Alps, and French coast. High spatial resolution is used to resolve small-scale features such as gravity waves and wave steepening over terrain. There are 30 vertical levels and the terrain-following coordinate is stretched with $\delta Z_{\min} = 20 \text{ m}$ near the surface. The model top is at 31 km with Rayleigh damping applied to the upper 11 km. The initial and boundary conditions are specified using NOGAPS analysis and forecast fields. For the two mistral simulations, the model was initialized at 1200 UTC, 30 September and 0000 UTC, 6 November respectively.

(b) Model testing and the simulated mistral patterns

Extensive comparisons between simulations and observations were made to examine the performance of the COAMPS model. Generally, COAMPS shows satisfactory skill in predicting the timing and strength of the mistral wind, the stationary MCCL, the persistent MLBC, and the structure of the MESL. A comparison of the COAMPS and flight-level data is shown in Figs. 9(a) and (b).

The geostrophic wind normal to the flight track is derived from the measured pressure corrected to a constant height using the hydrostatic approximation and the derived v_g was smoothed over 200 points. The COAMPS model winds at the flight level and at the approximate flight time are shown as well. For the first mistral, COAMPS winds agree with the observations quite well except that the shear zone predicted by COAMPS was broader. The geostrophic winds derived from the COAMPS and the flight

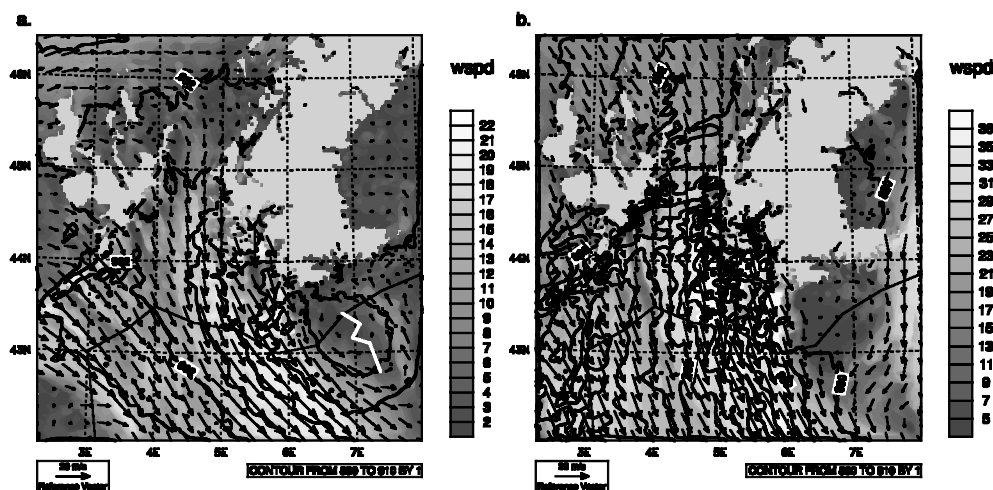


Figure 10. Snapshots of wind and pressure at $Z = 1$ km from the Coupled Ocean Atmosphere Mesoscale Prediction System (COAMPS) simulations. Pressure (mbar) is contoured and wind speed (m s^{-1}) is given by the grey scale. Arrows are wind vectors. (a) 1230 UTC, 1 October 1999. The white line indicates the Mistral Eastern Shear Line (MESL) detected by the NOAA P-3 belly radar (see text); (b) 1800 UTC, 6 November 1999.

data show even better agreement. The agreement for the second leg of the 6 November case was not as good, probably due to the unsteady nature of the second mistral. Still, the COAMPS model captured the strong mistral wind (but was 20% weaker), and the sharp shear zone (but was shifted half a degree westward).

To give readers a general idea of the simulated mistral wind field, the wind and pressure fields at the 1 km level are shown in Fig. 10. For 1230 UTC, 1 October (Fig. 10(a)), the strong mistral wind originated from the north end of the Rhône Valley with a cyclonic curvature and extended beyond the south boundary of the inner domain. The western boundary of the mistral was defined by a narrow wake trailing downstream from Mont Lozère (hereafter referred to as the Mont Lozère Wake (MLW)). To the east, a sharp shear line (MESL) separated the strong mistral wind from mountain wakes trailing from de Lure and Alpes Maritimes peaks. The high-wind zone was more than 300 km long and about 150 km wide with wind speed over 22 m s^{-1} near Toulon. Upstream of the mistral (near Lyon), the wind was much weaker ($< 5 \text{ m s}^{-1}$). The COAMPS also shows a flow reversal to the east of the MESL, which agrees with observations (Fig. 7(a)). The white curve marked a boundary in sea surface roughness detected by the P-3 belly radar (0930 UTC, 1 October) where the echo returns dropped sharply from more than 32 dBZ to less than 20 dBZ.

The second mistral was much stronger than the first one, with a maximum wind speed near 40 m s^{-1} (Fig. 10(b)). The location of the wind maximum was to the west of Nice, onshore prior to 1500 UTC, and shifted offshore afterward. The pressure field contained some high-frequency modes, due to gravity waves launched from irregular terrain in response to the stronger low-level wind. The shear line (MESL) was sharper and there was no wind reversal to the east of the MESL. Instead, there was a fairly strong north-easterly jet, which is in agreement with observations (Fig. 9(b)). The weak wind upstream of the Rhône Valley seen in Fig. 10(a) did not appear, implying less blocking. Again, to the west, the mistral was bounded by the MLW and to the east by wakes trailing from Alpes Maritimes peaks.

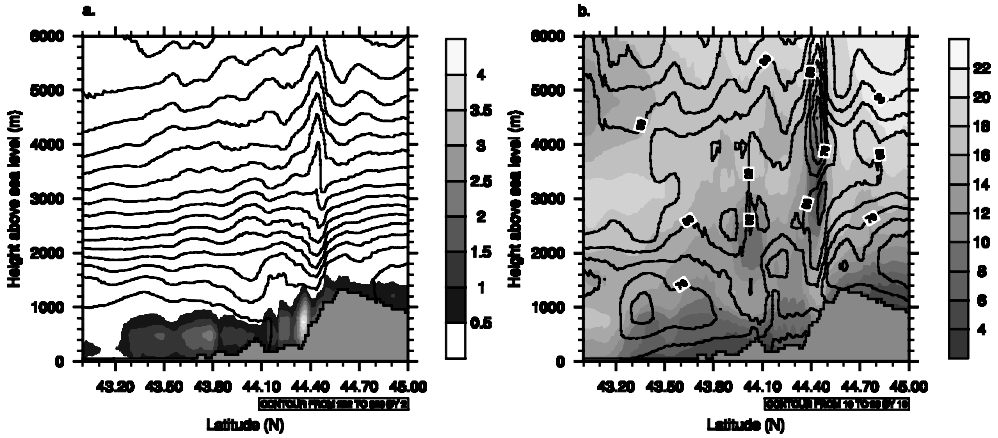


Figure 11. Vertical section across line aa at 1230 UTC, 1 October 1999. (a) Potential temperature (K) contours and turbulent kinetic energy (m^2s^{-2} , grey scale). (b) Relative humidity (%) contours and wind speed (m s^{-1} , grey scale).

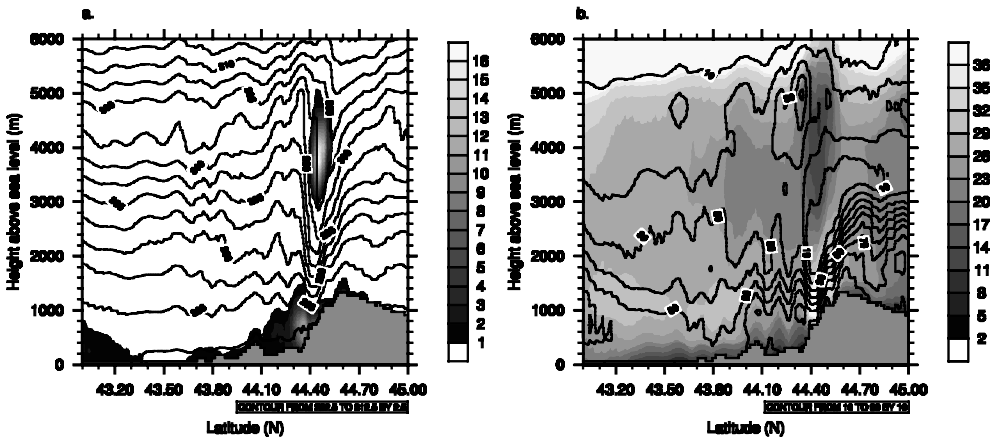


Figure 12. Same as Fig. 11 except for 1800 UTC, 6 November 1999.

(c) Gravity-wave breaking and wake formation

According to COAMPS simulations, the wake(s) trailing from Mont Lozère (MLW) defined the western boundary of the mistral and separated the mistral wind from the Tramontane jet. These wakes were long and persistent. However, questions arise regarding the mechanisms of the wake formation and the structure of MLW.

To examine the structure of these wakes, vertical sections were selected along the wind direction. Potential temperature, TKE, wind speed, and relative humidity in a vertical section cutting through Mont Lozère and oriented along the wind direction (aa, see Fig. 5(a)) are shown in Figs. 11 and 12. Figure 11(a) indicates that the low-level moist flow was blocked by the peak. There is a hydraulic jump, i.e. a steepening gravity wave coincident with a TKE maximum (~ 800 m ASL), below the stable layer and downstream of Mont Lozère. Associated with the hydraulic jump, the low-level wind speed decreased from 10 m s^{-1} to about 4 m s^{-1} near the ground. Flow above the stable

layer responded in an opposite phase as found in two-layer flow (Jiang and Smith 2003). Along the wind direction, flow descent across the Mont Lozère was evident. There is a sharp decrease of RH associated with flow descent and warming (Fig. 11(b)).

The potential temperature, TKE etc. for 1800 UTC, 6 November are shown in Fig. 12. As expected, the windward blocking was much weaker and wave response was much stronger than the 1 October event due to the much larger cross-mountain wind speed. A large-amplitude wave extended to 6 km above the sea level with two separate TKE maxima: one below, and the other above the relatively stable layer. This type of wave breaking has been classified as external jump by Jiang and Smith (2003). Associated with gravity-wave breaking, the wind speed was decelerated downstream of the TKE maxima. Relative humidity of the low-level air decreased from 90% to 30% across Mont Lozère.

The plan views of the RH field (not shown) at 1 km and 2 km ASL also show banner 'clouds' (i.e. $RH > 85\%$) over the Mont Lozère wake as observed from space during both mistral events. To examine the connection between the wakes and the banner clouds (MLBC), vertical sections of RH, w , TKE, and potential temperature across the MLW are analysed (not shown). While no distinguishable vertical motion is observed in the wake, the boundary-layer top, defined by the stable layer and a sharp decrease of TKE and RH, was about 200–300 m higher over the MLW during both mistral events. As is well known, isentropes ascend rapidly in a jump and remain elevated after the hydraulic jump. Along the MLW, there was an increase of RH in the boundary layer over the sea surface, probably associated with turbulent mixing of water vapour from the sea surface. Based on these observations, the formation of the banner clouds (MLBC) was probably due to less descent of air after the hydraulic jump, and turbulent mixing in the wake which may have transported moisture from the sea surface to a higher level.

Another pair of sections cutting through the French Alps (not shown) indicated that the underlying terrain was extremely complex with massive wave breaking and corresponding TKE clusters. Generally, wave breaking was stronger and deeper for the 6 November event. Low-level wave breaking (i.e. hydraulic jump) was located downstream of the French Dauphine as well as for the first mistral event. The connection between mountain wakes and hydraulic jumps has been noticed by previous studies (e.g. Smith *et al.* 1997; Rotunno *et al.* 1999).

Many western Alpine massifs are above 3 km and known for strong wave activity. This study suggests that even over low terrain such as peaks of the Massif Central and the French Dauphine, massive wave breaking can occur during strong mistral periods. For the second mistral event, wave breaking reached above 6 km with maximum vertical motion of 6 m s^{-1} . Mountain waves and wave-breaking-induced turbulence may pose a threat to small aircraft and sometimes even commercial jets. According to the simulations, wave breaking occurred over the following peaks: Mts de Lacaune (43.65°N , 2.6°E , 1266 m), Mt Aigoual (44.2°N , 3.5°E , 1567 m), de Lure (44.2°N , 5.7°E , 1827 m), Mont Ventoux (44.25°N , 5.28°E , 1909 m), Mont dela Bernarde (43.7°N , 6.65°E , 1941 m), and Mt Cheiron (43.8°N , 6.95°E , 1776 m). Mountain waves in this region were observed by previous studies (Gerbier and Berenger 1961).

(d) Trajectory analysis

Trajectories are computed using the three-dimensional model wind interpolated in space and time. The time interval is 30 s. Trajectories are allowed to run through turbulent regions and terminate whenever they are below the surface. To examine the nature and history of the air parcels encountered along the flight track and across the MESL, nine air parcels were 'launched' along the flight track and at 1 km ASL

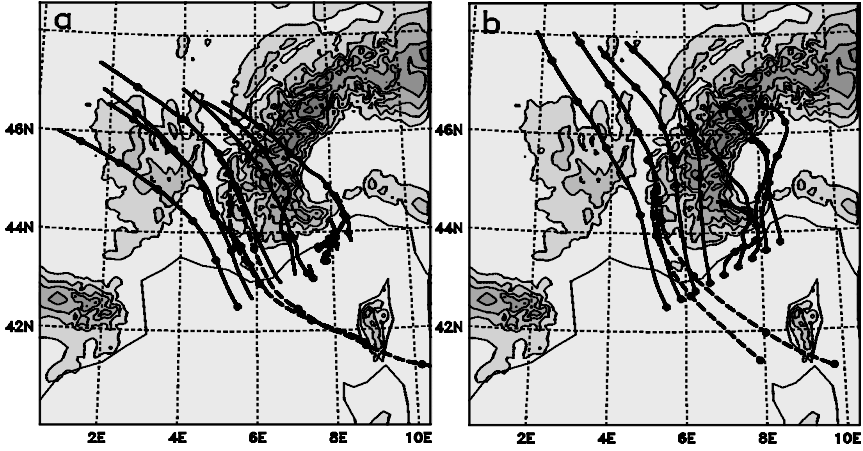


Figure 13. Plan view of trajectories and terrain field. Two groups of trajectories are shown: backward trajectories of nine parcels (1) launched from the flight track, 1000 m above sea level (ASL) (solid); and forward trajectories of two parcels (2) launched from point (5°E , 45.5°N), 500 m ASL and 1000 m ASL (dashed). (a) The first mistral event. Group 1 was launched at 1230 UTC and group 2 was launched at 0130 UTC. (b) The second mistral event. Group 1 was launched at 1800 UTC and group 2 was launched at 1200 UTC.

at 1230 UTC, 1 October and 1800 UTC, 6 November, respectively. The backward trajectories of these parcels are shown in Figs. 13(a) and 13(b). If we number the trajectories from west to east, Fig. 13(a) shows that the first three turned southward as they approached the western Alps and then either ascended over the Massif Central or turned into the Rhône Valley. The middle three (4, 5 and 6) ascended over the relatively lower peaks of the French Dauphine (1.5–2 km) or the Alpes de Provence (1.5–2 km). Parcel 7 arrived from north of the Alps through ascent over the central Alpine ridge and avoidance of the high peaks of Alpes Maritime (3 km). Parcels 6 and 7 indicated a wind reversal. Another pair of forward trajectories of parcels launched from point (5°E , 45.5°N) at 0130 UTC 1 October, and from 500 m and 1000 m ASL respectively are shown as dashed lines. The 500 m parcel was slow at the beginning (the time between two neighbouring dots is 2 hours) and accelerated rapidly down the Rhône Valley. At roughly 0930 UTC, it reached the coast and its speed was close to the 1000 m parcel off the coast line. The 1000 m parcel was faster and experienced less turning over the land. Both parcels turned cyclonically prior to reaching the Strait of Bonifacio.

Figure 13(b) depicts consistent characteristics. For the first two trajectories (from the west along the flight track), the air parcels were channelled into the Rhône Valley. Parcels 3 and 4 ascended and passed over the French Dauphine or the Alpes de Provence. The other five originated from the Po Valley. No flow reversal occurred. The two forward trajectories of parcels launched at the entrance of the Rhône Valley at 1200 UTC indicated much stronger wind and cyclonic curvatures.

Some properties along the paths of parcels 2 and 6, launched from the 1 km level, are plotted in Fig. 14. For the first mistral, parcel 2 arrived from north of the Massif Central about 2.25 km ASL. It encountered some low terrain (<1 km) along its path and descended more than 1 km (Fig. 14(a)) by the time it reached the flight track. The v component of wind increased correspondingly from about 7 m s^{-1} to 16 m s^{-1} . In Fig. 14, the meridional component of the geostrophic wind (i.e. $v_g = -(\rho f)^{-1} \partial p / \partial x$, where ρ is the air density and the derived v_g was smoothed over 200 points) is plotted for comparison. It is interesting that during the course of turning, v_g was much smaller

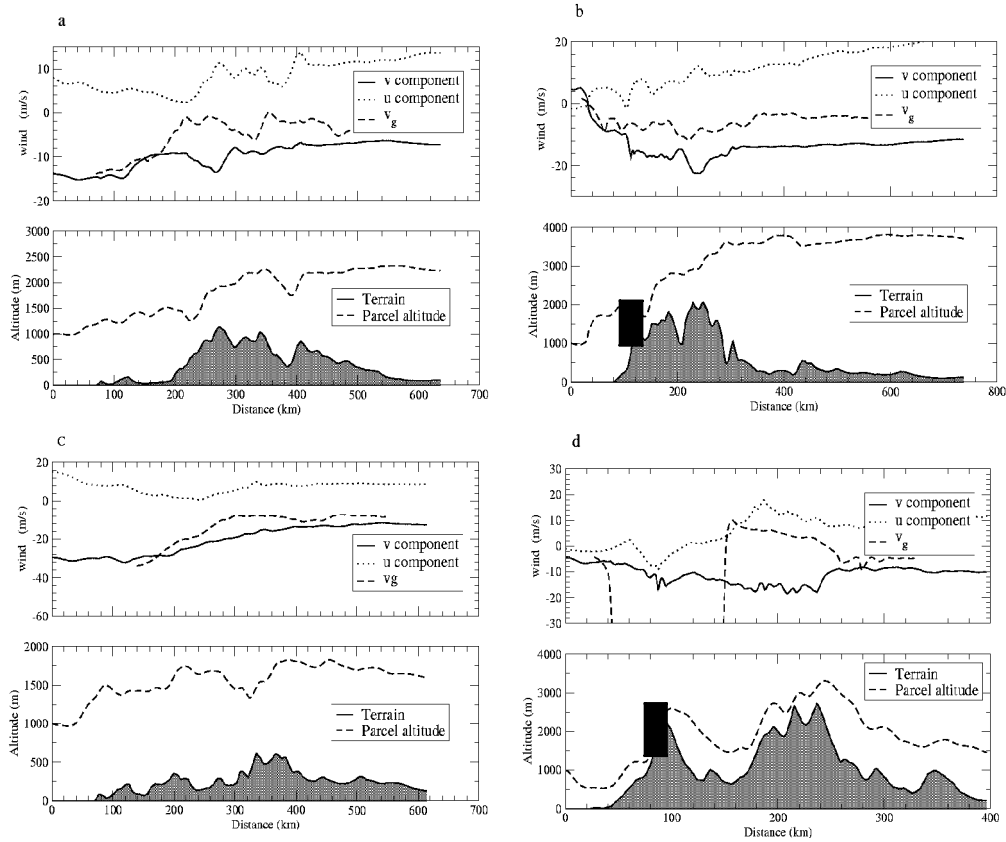


Figure 14. Properties of four trajectories ending at the aircraft track at $Z = 1$ km. The horizontal axis is the distance upwind along the trajectory. Upper panel: u (solid) and v (dashed + dot) component of wind (m s^{-1}), north–south component geostrophic wind (dashed); lower panel: terrain and parcel altitude. Black boxes indicate segments with turbulent kinetic energy larger than $1 \text{ m}^2 \text{ s}^{-2}$. (a) 1 October, parcel 2 (5.9°E , 42.7°N , $Z = 1$ km), (b) 1 October, parcel 6 (7.38°E , 43.3°N , $Z = 1$ km), (c) 6 November, parcel 2, (d) 6 November, parcel 6.

than v ($v/v_g > 3$). Therefore, the turning of this parcel was not forced by the pressure-gradient force, but, primarily by the Coriolis force. The large-scale pressure-gradient force was predominantly cancelled by the perturbation pressure-gradient force near the Alps. By the time the parcel reached the coast, it returned to approximate geostrophic balance due to a rapid increase of the pressure-gradient force. Further downstream, the pressure-gradient force became dominant as suggested by the cyclonic turning of the mistral wind.

Parcel 6 originated from a higher altitude (~ 4 km, Fig. 14(b)). Prior to reaching the flight track, it encountered some moderate terrain (2 km) such as the French Dauphine and descended to 1 km. Along the path, the v component increased from 10 m s^{-1} to more than 15 m s^{-1} over the slope of the Alpes de Provence. Then it experienced a sharp deceleration from 20 m s^{-1} to 0 in less than 100 km in response to the dissipation possibly associated with a hydraulic jump (see Fig. 14(b), TKE cluster indicated by a black box, and the corresponding steep trajectory and sharp decrease of wind). Flow reversal occurred over the sea surface.

For the second mistral, parcel 2 managed to propagate through the Rhône Valley. It encountered only low terrain (~ 500 m) and experienced a descent of about 800 m

(Fig. 14(c)). During this period, the parcel was accelerated from 15 m s^{-1} to 30 m s^{-1} . There was some turning towards the right, associated with the unbalanced Coriolis force as well. Parcel 6 ascended over some major peaks ($\sim 3 \text{ km}$) and the wind speed decreased sharply in response to dissipation over the lee slope of the last peak (Fig. 14(c), TKE cluster indicated by a black box). The trajectory showed some ascent near the dissipative region but not as sharp as seen in Fig. 14(b). The dissipation was more likely related to boundary-layer turbulence. It should be pointed out, however, that three-dimensional animations clearly indicated steepening large-amplitude gravity waves coincident with TKE clusters over the western Alps. Therefore, the formation of the Western Alps Wake (WAW) should be associated with both turbulent dissipation induced by wave breaking and boundary-layer friction.

In summary, trajectory analysis indicated that the different air parcels along the flight track had quite different histories and characteristics. Parcels to the west of the MESL turned to the right under the influence of the Coriolis force and experienced little dissipation. Acceleration and descent occurred along their paths. In the examples shown above, parcel 2 had similar histories for both mistral events (Figs. 14(a),(c)). It approached the Alps in balance, was thrown out of balance by terrain-induced perturbations, and adjusted itself to a new balance over a short distance. The Rossby radius of deformation ($R = U/f$) was around 150 km for the 1 October case, and around 300 km for the 6 November case. In Fig. 14(a), the parcel reached a new balance over about 50 km , and in Fig. 14(c), the parcel reached a new balance in about 150 km . This fast adjustment implied that it was not a typical geostrophic adjustment. Instead, the adjustment process can be described as inertial flow propagating into a prescribed pressure field and achieving a new balance by coincidence. This coincidental balance did not last long. As shown in Fig. 9, further downstream, the pressure-gradient force dominated, and parcels began to turn cyclonically.

7. CONCLUSIONS

Some phenomenological and mechanistic aspects of the mistral wind are investigated using observational data and high-resolution mesoscale simulations. The COAMPS simulations were in satisfactory agreement with observations. The findings are illustrated in Fig. 15.

Both mistral events were associated with the passage of a cold front which directed cold air toward the western Alps and Massif Central from the north-west. During both events, the mistral flow was beneath a thin stable layer with drier and potentially warmer air above the stable layer. This structure was associated with flow descent after the passage of a cold front.

A stationary cloud-clearing line (MCCL) was located over the lee of the Massif Central and was associated with the acceleration of the mistral wind according to COAMPS. To the west, the mistral wind was separated from the Tramontane wind by the MLW created by a hydraulic jump over the lee of the Mont Lozère. The narrow and persistent MLW may extend more than 100 kilometres downstream with banner clouds (MLBC) above it. The formation of the MLBC is probably due to the deeper turbulent boundary layer in the wake associated with the jump and turbulent mixing of moisture from the sea surface. To the east, a sharp shear line (MESL) separated the mistral wind from the WAW. The formation of the WAW was rather complicated. According to COAMPS, possible mechanisms include dissipation due to hydraulic jumps and boundary-layer turbulence.

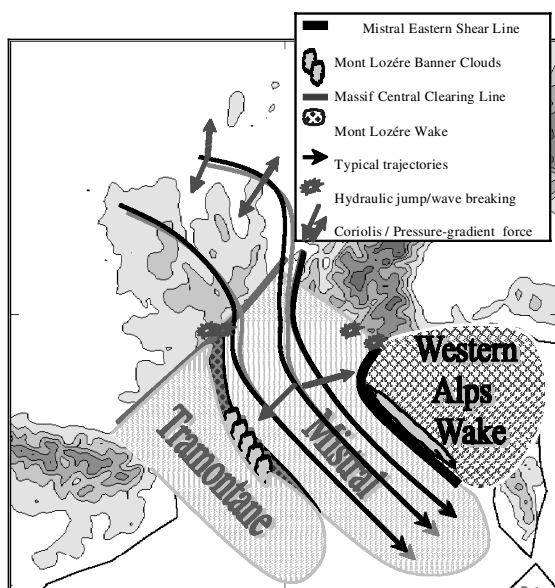


Figure 15. Summary diagram depicting features of the mistral wind.

Two types of wind turning were identified from the COAMPS simulations. One was low-level flow blocking by the Alps, which built up a cold-air reservoir. The cold air leaked through the entrance of the Rhône Valley and was accelerated into the mistral. Further aloft, inertial turning occurred due to a cancellation between the large-scale pressure gradient and perturbation pressure gradient introduced by the western Alps. Near the coast, the pressure-gradient force became dominant and the mistral wind turned cyclonically. Some of these features were noted by Chen and Smith (1987).

In the literature, the mistral has been often referred to as a ‘gap wind’, a ‘fall wind’, or a wind that develops down the Rhône Valley (Glickman 2000). The results of this study suggest that the mistral wind can be partly described by the above terms, but none of them accurately capture the full range of mistral dynamics. For example, for the 1 October case, a large portion of the mistral flow actually ascended and passed over the Massif Central, and the term ‘fall wind’ is more accurate in that sense. However, Lyon is only 240 m ASL and for the blocked air or air channelled into the Rhône Valley, ‘gap’ wind might be a better description. Our study also implies that the mistral is deep enough to override some of the terrain and wide enough for the Coriolis force to be important. Considering the importance of wakes induced by hydraulic jump in shaping the mistral wind, we conclude that the formation of the mistral wind is clearly related to multiscale dynamics.

ACKNOWLEDGEMENTS

This research was supported by the National Science Foundation, Division of Atmospheric Sciences (ATM-0112354). Dr S. Skubis helped with some figures. The research for the third author was provided by the Office of Naval Research (ONR) program element 0601153N. Computing time was supported in part by a grant of High Performance Computing (HPC) time from the Department of Defense Major Shared Resource Center, at Vicksburg, MS, and Aberdeen, MD. The data for the field program

was collected in a joint effort by the MAP scientists and staff, especially our colleagues in the potential-vorticity banner group; Dr C. Schär, Dr V. Grubišić, Dr L. Nance, Dr S. Skubis, Dr C. Flament, Dr M. Ralph, etc. The simulations were made using COAMPS developed by US Naval Research laboratory. The authors would like to thank two anonymous reviewers for their constructive comments and suggestions.

REFERENCES

- Aebischer, U. and Schär, C. 1998 Low-level potential vorticity and cyclogenesis to the lee of the Alps. *J. Atmos. Sci.*, **55**, 186–207
- Bordreuil, C., Barbia, A. and Comte, P. 1973 'Vent du Nord-Ouest et mistral a Marseille de 1982 a 1970'. Monographie 88 de la Meteorologie Nationale
- Bougeault, P., Binder, P., Buzzi, A., Dirks, R., Houze, R., Kuettner, J., Smith, R. B., Steinacker, R. and Volkert, H. 2001 The MAP Special Observing period. *Bull. Am. Meteorol. Soc.*, **82**, 433–462
- Campins, J., Jansa, A., Bench, B., Koffi, E. and Bessemoulin, P. 1995 PYREX observation and model diagnosis of the Tramontane wind. *Meteorol. Atmos. Phys.*, **56**, 209–228
- Chen, W. and Smith, R. B. 1987 Blocking and deflection of airflow by the Alps. *Mon. Weather Rev.*, **115**, 2578–2597
- Galzi, L. 1952 Contribution a l'etude du mistral. *La Meteorologie*, **13**, 7–24
- Gerbier, N. and Berenger, M. 1961 Experimental studies of lee waves in the French Alps. *Q. J. R. Meteorol. Soc.*, **87**, 13–23
- Glickman, T. S. 2000 *Glossary of meteorology*. American Meteorological Society, Boston, USA
- Harshvardhan, Davies, R., Randall, D. and Corsetti, T. 1987 A fast radiation parameterization for atmospheric circulation models. *J. Geophys. Res.*, **92**, 1009–1015
- Hodur, R. M. 1997 The Naval Research Laboratory's Coupled Ocean/Atmosphere Mesoscale Prediction System (COAMPS). *Mon. Weather Rev.*, **125**, 1414–1430
- Jansá, A. 1987 Distribution of the mistral: A satellite observation. *Meteorol. Atmos. Phys.*, **36**, 201–214
- Jiang, Q. and Smith, R. B. 2003 Wave breaking in two layer flow. *J. Atmos. Sci.*, in press
- Mayencon, R. 1980 *Meteo Pratique. Neptune-Edition et d'Outre-Mer*. Paris, France
- Mellor, G. L. and Yamada, T. 1974 A hierarchy of turbulence closure models for planetary boundary layers. *J. Atmos. Sci.*, **31**, 1–28
- Pette, P. 1982 On the problem of violent valley winds. *J. Atmos. Sci.*, **39**, 542–554
- Rotunno, R., Grubišić, V. and Smolarkiewicz, P. K. 1999 Vorticity and potential vorticity in mountain wakes. *J. Atmos. Sci.*, **56**, 2796–2810
- Schär, C., Sprenger, M., Lüthi, D., Jiang, Q., Smith, R. B. and Benoit, R. 2003 Structure and dynamics of an Alpine potential-vorticity banner. *Q. J. R. Meteorol. Soc.*, **129**, 825–855
- Schott, F., Visbeck, M., Send, U., Fischer, J., Stramma, L. and Desaubies, Y. 1996 Observations of deep convection in the Gulf of Lions, northern Mediterranean, during the Winter of 1991–92. *J. Phys. Ocean.*, **26**, 505–524
- Smith, R. B. 1987 Aerial observations of the Yugoslavian bora. *J. Atmos. Sci.*, **44**, 269–297
- Smith, R. B., Gleason, A., Gluhosky, P. A. and Grubišić, V. 1997 The wake of St Vincent. *J. Atmos. Sci.*, **54**, 606–623
- Wrathall, J. E. 1985 The mistral and forest fires in Provence, Cote d'Azur, South France. *Weather*, **40**, 119–124